remote sensing

MDPI

Technical Note

The InSAeS4 Airborne X-Band Interferometric SAR System: A First Assessment on Its Imaging and Topographic Mapping Capabilities

Stefano Perna [1,2], Carmen Esposito [1,3], Tiago Amaral [4], Paolo Berardino [1], Giuseppe Jackson [1,2], João Moreira [4], Antonio Pauciullo [1], Eurico Vaz Junior [4], Christian Wimmer [4] and Riccardo Lanari [1,*]

Received: 26 November 2015; Accepted: 30 December 2015; Published: 6 January 2016
Academic Editors: Richard Gloaguen and Prasad S. Thenkabail

[1] Istituto per il Rilevamento Elettromagnetico dell'Ambiente (IREA)—Consiglio Nazionale delle Ricerche (CNR), Napoli 80124, Italy; perna@uniparthenope.it (S.P.); esposito.c@irea.cnr.it (C.E.); berardino.p@irea.cnr.it (P.B.); jackson.g@irea.cnr.it (G.J.); pauciullo.a@irea.cnr.it (A.P.)
[2] Dipartimento di Ingegneria (DI), Università degli Studi di Napoli "Parthenope", Napoli 80143, Italy
[3] Dipartimento di Ingegneria (DING), Università degli Studi del Sannio, Benevento 82100, Italy
[4] Bradar Indústria S/A, São José dos Campos (SP), 12244-000, Brazil; tiago.amaral@bradar.com.br (T.A.); joao.moreira@bradar.com.br (J.M.); eurico.vaz@bradar.com.br (E.V.J.); christian.wimmer@bradar.com.br (C.W.)
* Correspondence: lanari.r@irea.cnr.it; Tel.: +39-081-762-0612

Abstract: We present in this work a first assessment of the imaging and topographic mapping capabilities of the InSAeS4 system, which is a single-pass interferometric airborne X-Band Synthetic Aperture Radar (SAR). In particular, we first provide a brief description of the InSAeS4 sensor. Then, we discuss the results of our analysis on the SAR and interferometric SAR products relevant to the first flight-test campaign. More specifically, we have exploited as reference the GPS measurements relevant to nine Corner Reflectors (CRs) deployed over the illuminated area during the campaign and a laser scanner Digital Elevation Model (DEM). From the analysis carried out on the CRs we achieved a mean geometric resolution, for the SAR products, of about 0.14 m in azimuth and 0.49 m in range, a positioning misalignment with standard deviation of 0.07 m in range and 0.08 m in azimuth, and a height error with standard deviation of 0.51 m. From the comparison with the laser scanner DEM we estimated a height error with standard deviation of 1.57 m.

Keywords: Synthetic Aperture Radar (SAR); airborne SAR; airborne SAR Interferometery; Digital Elevation Model (DEM)

1. Introduction

Synthetic Aperture Radar (SAR) Interferometry (InSAR) is a well-known technique that allows the generation of the Digital Elevation Model (DEM) of an area through the exploitation of the phase difference (interferogram) between SAR data pairs relevant to the same observed scene and received from slightly different view angles [1,2].

SAR sensors can be mounted on satellites, space-shuttles, airplanes, helicopters and ground stations. In the former case, the images and the corresponding interferometric products are characterized by a wider spatial coverage coupled to a geometric resolution typically lower than that achievable in the other cases, where smaller antennas can be exploited [1]. In all the cases, the InSAR configurations can be obtained either by means of repeated passes of the sensor over the same area or by exploiting multiple antennas forming a single-pass system [1].

As for the spaceborne systems, the generation of InSAR products is a relatively assessed task, due to the high stability of the orbits covered by the platforms. Indeed, this kind of acquisition geometry simplifies the SAR focusing step and the subsequent InSAR processing chain [1]. With particular reference to the DEM generation, the temporal decorrelation effects [1] may be very severe in repeat-pass spaceborne acquisitions; single-pass systems are therefore preferred. For instance, the worldwide SRTM DEM has been obtained through a space shuttle mission that exploited a single-pass configuration [3]. Moreover, the current TanDEM-X mission [4] exploits two satellite platforms to form a single-pass configuration aimed at obtaining a worldwide product with resolution higher than that of the SRTM DEM.

Turning to the airborne systems, in principle all of them allow carrying out repeat-pass InSAR. Indeed, due to the operational flexibility peculiar to the airborne platforms, the revisit time between two repeated passes can be kept very short, thus strongly limiting the decorrelation effects typical of spaceborne repeat-pass systems. However, differently from the spaceborne case, the generation of repeat-pass airborne InSAR products is not a turn of the crank procedure. This is due to the platform deviations from a rectilinear, reference flight track. Indeed, such track deviations, which are induced by atmospheric turbulences and winds, produce on the received data so called motion errors [5], which need to be properly compensated. To this aim, proper algorithms implementing the so called Motion Compensation (MOCO) [6,7] procedure must be applied. In particular, their implementation requires the knowledge of the sensor positions during the acquisition and the availability of an external DEM of the observed area. Accordingly, the effectiveness of such MOCO algorithms can be impaired on one hand by the limited precision of the navigation unit mounted on board, and on the other hand by the inaccuracy of the available external DEM [5]. In addition, in order to efficiently account for the space-variant nature of the motion errors, some approximations are usually applied during the MOCO procedure [8]. For these reasons, the focused airborne SAR data are typically affected by the so called residual motion errors [5], not compensated by the MOCO procedure. In particular, the most critical residual motion errors are those induced by the navigation unit inaccuracies [9]. To this regard, it must be underlined that such errors become less critical in single-pass InSAR systems, since they are quite similar in the different interferometric channels and therefore tend to cancel each other during the InSAR pair beating. Differently, in the repeat-pass airborne InSAR systems, the residual MOCO errors may severely impair the accuracy of the final interferograms, especially when high frequency systems (namely, operating from C- to Ka-bands) are employed. For these reasons, airborne repeat-pass InSAR DEMs are typically generated with low frequency systems, such as the P-Band OrbiSAR one [10], which employ wavelengths that are quite large if compared with the typical positioning errors of the modern navigation units. To this regard, it is also stressed that low frequency systems may hardly work in a single-pass airborne configuration. Indeed, to keep the height of ambiguity [2] of the interferometric configuration sufficiently low, the appropriate InSAR baseline would be too large with respect to the fuselage of airplanes typically exploited for SAR missions. Notwithstanding, some examples of single-pass airborne systems operating at low frequencies exist (consider for instance the P-Band GeoSAR [11]).

More generally, single-pass airborne InSAR systems typically exploit higher frequencies. Examples of such systems are the C-/X-Band F-SAR [12], the X-Band PAMIR [13], the X-/Ku-Band RAMSES [14], the X-Band SETHI [15], the X-Band OrbiSAR [9] and the Ka-Band MEMPHIS [16–20]. As a matter of fact, in these systems the InSAR baseline can be as small as required by the geometrical constraints imposed by small airborne platforms. As observed above, in such single-pass systems, the residual motion errors affecting the focused data are typically not negligible at the employed frequencies; however, they tend to cancel each other in the corresponding interferograms.

In this work, we present a first assessment of the imaging and topographic mapping capabilities of the X-Band InSAeS4, which is an Italian single-pass interferometric airborne SAR system. More specifically, the InSAeS4, also named TELAER [21], is owned by the Italian Agency for Agriculture Subsidy Payments (AGEA) and upgrades the AeS4 system, which was equipped with a single

antenna. More specifically, the original AeS4 system has been upgraded to a single-pass interferometric configuration thanks to a funding of the Italian Ministry of Education, Universities and Research (MIUR), through the Italian National Research Council (CNR), in the frame of a cooperation between CNR and AGEA. The system upgrade has been developed by the Institute for the Electromagnetic Sensing of the Environment (IREA), of CNR, and implemented by Orbisat (now Bradar). Thanks to this upgrade, the InSAeS4 system is now equipped with an interferometric layout consisting of three antennas installed in order to allow the simultaneous presence of three Across-Track (XT) baselines for the generation of DEMs [1,2], and three Along-Track (AT) baselines mainly for sea surface velocity measurements.

In this work we first provide a description of the InSAeS4 system. Then, we present the results relevant to the acquisition campaign carried out in 2013 just after the ending of the system upgrade. Our analysis is aimed at presenting a first assessment of the imaging and topographic mapping capabilities of the InSAeS4 sensor, in order to provide reference values for future research activities involving the use of the data acquired by this sensor. In particular, we first investigate the imaging capability of the focused data. Then, we concentrate on the characteristics of the single-pass XT InSAR products and present a quantitative assessment of the accuracy of the generated single-pass DEM. To this aim, we provide comparisons with both Differential GPS (DGPS) measurements on Corner Reflectors (CRs) and a laser scanner DEM.

2. System Description

The InSAeS4 system is mounted onboard a Learjet 35A, whose main parameters are collected in Table 1. The description of the main modules of the system is provided in the following subsections.

Table 1. Airplane parameters.

Model	LearJet 35A
Propulsion	2 Turbofan Garret T731
Velocity	up to 800 km/h
Autonomy	4000 km
Altitude	up to 8.4 km

2.1. Navigation Unit

In order to limit the effects of residual motion errors, which unavoidably affect the MOCO procedures, the system upgrade has involved the acquirement of an embedded GNSS-IMU equipment: the Applanix POS-AV 510. Indeed, the use of this navigation unit, coupled to proper post flight processing techniques, guarantees very precise flight parameter measurability, see Table 2.

Table 2. Absolute Accuracy Specifications (RMS) of the upgraded IMU *.

Position	0.05 m
Velocity	0.005 m/s
Roll & Pitch	0.005°
True Heading	0.008°

* after post-processing integration with GNSS data.

2.2. Antennas

The three antennas of the InSAeS4 system are X-Band horn arrays, looking to the right with 45° of elevation tilt. Each antenna is an array of four standard pyramidal horns mounted in a 21.6 × 13.4 × 12.2 cm radome with an overall weight of 4.9 kg.

The antenna parameters, which have been measured in the anechoic chamber, are practically the same for the three antennas. In particular, the gain [22] is equal to 20.7 dB whereas the half power beamwidth [22] is equal to 35° in the range direction and 7.6° in the azimuth one. When considering the squared pattern (to account for the two-way signal path) these values decrease to 25° and 5.6°, respectively. In particular, from the latter value we obtain a half power Doppler bandwidth equal to 778 Hz when considering the operating velocity of the Learjet 35A (approximately equal to 125 m/s).

It is finally remarked that for each antenna the accurate calculation of the phase center position has been carried out in the anechoic chamber, as shown in [23].

2.3. Radar

The InSAeS4 radar (whose main parameters are collected in Table 3) consists of three X-band interferometric channels. In particular, it is possible to activate all the three channels, obtaining a multi-baseline interferometric configuration, or just a part of them, obtaining a two-antennas configuration or the single antenna configuration of the original AeS4 system. The hardware upgrade leading from the original AeS4 to the InSAeS4 system has not involved the installation of additional transmitters and receivers. Thus, the interferometric configuration is obtained by means of a low-power multiplexer that carries out the proper antenna switching. This involves the following implications on the system settings and performances.

Table 3. Radar parameters.

Peak Transmit Power	2600 W
Duty cycle	up to 6%
Carrier frequency	9.55 GHz
Carrier wavelength	0.0314 m
Bandwidth	50–400 MHz
PRF	0.2–16 kHz
Recording data rate	up to 32 MB/s
Number of antennas	3
Polarization	HH

First, to achieve a given azimuth data sampling it is necessary to increase the radar Pulse Repetition Frequency (PRF) of a factor equal to the number of activated interferometric channels. Therefore, the time required to record each received echo must be reduced by the same factor. Accordingly, when passing from the single antenna to the multi-antennas configuration, a reduction of the recordable range samples (and, therefore, of the across-track swath) is necessary in order to safely meet both the 32 MB/s limit imposed by the A/D conversion step and the 6% duty cycle limit.

The system exploits the stepped chirp technology [24], which permits to achieve up to 400 MHz of bandwidth by exploiting four chirp pulses of 100 MHz bandwidth at different carrier frequencies.

Note that in the 400 MHz case, with the multi-baseline configuration (all the three interferometric channels activated), we are capable to record a number of range samples leading to a (slant) range swath of 1.5 km. On the other side, it is in principle possible to reduce the overall bandwidth of the transmitted signal up to 50 MHz, obtaining a corresponding increase of the recordable range swath. In particular, considering again the multi-baseline interferometric configuration, in the 50 MHz case it is possible to record a (slant) range swath as wide as 12 km.

In this sense, the system is quite flexible. Indeed, although designed to achieve high resolution products (namely, 400 MHz of overall bandwidth), it can be tuned in order to operate with smaller bandwidths and with different interferometric configurations, PRFs, pulse lengths and across-track swaths. To this regard, it is noted that in the most critical case occurring with the 400 MHz bandwidth coupled with the multi-baseline interferometric configuration, the maximum system PRF (16 kHz) allows acquiring a Doppler bandwidth as wide as 1.3 kHz. This value, compared with the (half power) Doppler bandwidth imposed by the azimuth antenna pattern (see previous Section), guarantees a 67%

guard band with respect to the ideal Nyquist limit. This allows us to safely account for the spectral broadening of the acquired SAR data induced by the presence of attitude instabilities [1] and track deviations [5] of the airborne platform during the acquisition.

The InSAeS4 Noise Equivalent Sigma Zero (NESZ) [24] curves have been computed according to the antenna gain measurements carried out in laboratory and the radar component specifications. These curves are reported in Figure 1, for different flight altitudes and for the full-resolution (400 MHz) and low-resolution (50 MHz) acquisition modes. It can be seen that in the 400 MHz case, for all the considered flight altitudes, the NESZ curves are well below the −25 dB threshold in the entire angular region 20°–55°, which is wider than that actually recordable with the considered acquisition mode.

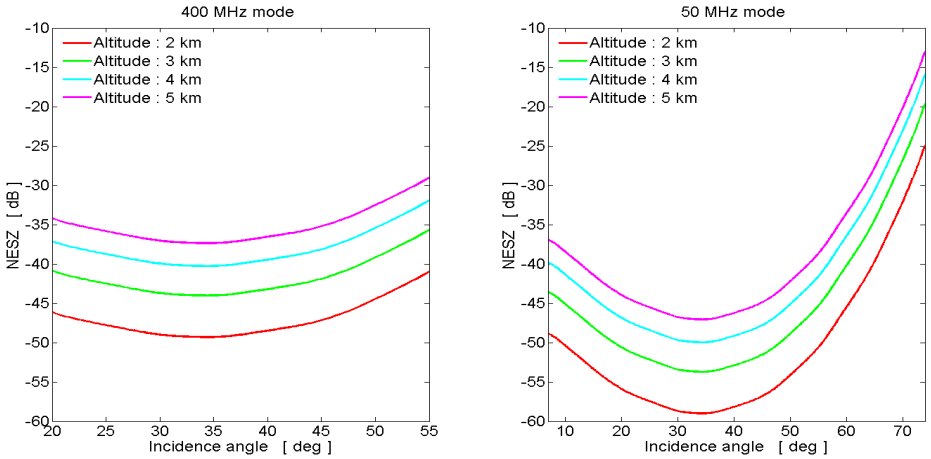

Figure 1. InSAeS4 Noise Equivalent Sigma Zero (NESZ) as a function of the incidence angle for the 400 MHz (**left**) and the 50 MHz (**right**) operational modes and for different flight altitudes.

Differently, in the 50 MHz case, the most critical NESZ curve lies below the −25 dB threshold only when the incidence angle is smaller than approximately 60°. On the other side, by forcing the far range at 60°, the exploitation of the entire recordable swath (which is 12 km wide) would involve coverage of the targets located at the nadir. To circumvent this problem, we could modify the NESZ curves by steering the antennas main lobe at a look angle greater than the current one (which is equal to 45°, see the previous Subsection, and it is optimally set for the 400 MHz mode). However, this procedure is difficult to implement since, at least currently, it could be achieved only mechanically. Thus, at the moment, the 50 MHz mode is coupled, in practice, to a range swath smaller than that actually recordable.

2.4. Interferometric Layout

The InSAeS4 system is equipped with an interferometric layout (shown in Figure 2) consisting of three antennas installed in such a way to allow the simultaneous presence of three XT and three AT baselines. Exploitation of the AT interferometric configuration is not addressed in this work, but it is worth for future discussion. In this case, we focus on the XT InSAR system capabilities. To this regard, we remark that the simultaneous availability of different XT baselines could be exploited to improve the accuracy of the final InSAR DEM, as shown in [4]. In our case, the three XT baseline components are 0.76 m, 0.93 m and 1.59 m, respectively. In particular, by considering as above the narrowest (1.5 km) and widest (12 km) recordable swaths (coupled to the 400 MHz and 50 MHz modes, respectively), a flight altitude of 4.5 km and an off-nadir angle of 30°, the three XT baselines lead to the heights of ambiguity summarized in Table 4. More specifically, the largest baseline leads to a height of ambiguity [2] ranging from 52 m to 114 m in the narrow swath case, and from 52 m to 611 m in the wide swath one. With the medium baseline, the height of ambiguity ranges from 101 m to 251 m in the narrow swath case, and from 101 m to 2151 m in the wide swath one. Finally, with the smallest

baseline, it ranges from 109 m to 208 m in the narrow swath case, and from 109 m to 853 m in the wide swath one.

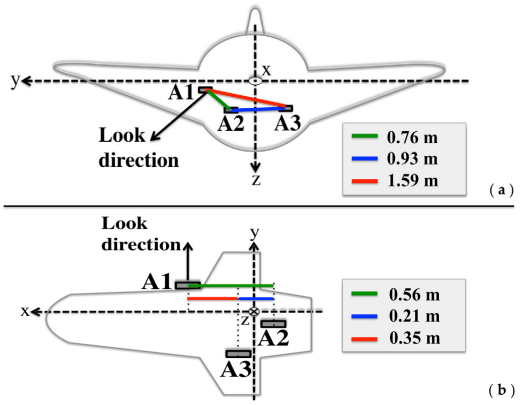

Figure 2. Interferometric layout of the InSAeS4 System. (**a**) Vertical (*i.e.*, across track) plane; (**b**) Horizontal plane. Note that the x-axis points ahead and z-axis points downward.

Table 4. Baseline *vs.* Height of ambiguity.

XT-Baseline	Height of Ambiguity 400 MHz Mode *	Height of Ambiguity 50 MHz Mode *
0.76 m	From 109 m to 208 m	From 109 m to 853 m
0.93 m	From 101 m to 251 m	From 101 m to 2151 m
1.59 m	From 52 m to 114 m	From 52 m to 611 m

* The reported values are relevant to a flight altitude of 4.5 km and an off-nadir angle of 30°.

3. Experimental Results

In this Section we present the results relevant to the first flight campaign carried out with the InSAeS4 system over the Napoli area, Italy, in January 2013, just after the completion of the interferometric system upgrade discussed above. In particular, amongst all the settable operational modes, we focus on the full-resolution acquisition mode (400 MHz), for which the system has been designed. Moreover, we also analyze the low-resolution acquisition mode (50 MHz). As shown in Figure 3a, we consider the three acquisitions (whose main parameters are summarized in Table 5) relevant to the Campi Flegrei Caldera area and the Somma-Vesuvio volcanic complex.

The frame 1 has been acquired with the 50 MHz mode with a single-baseline configuration obtained by activating only the two antennas separated by the largest XT baseline. The flight track is about 65 km long. In this case a 12 km (slant) range swath has been recorded with an off-nadir angle of 30°, which has led to a look angle of about 74° at far range. However, for this acquisition geometry, according to the NESZ curves of Figure 1 and the analysis of Section 2, we expect that only a part (corresponding approximately to the angular sector 30°–60°) of the recorded swath can be effectively exploited.

The frames 2 and 3 have been acquired with the 400 MHz mode by exploiting the multi-baseline configuration (that is, all the three antennas activated). In both cases, a 1.5 km (slant) range swath has been recorded with an off-nadir angle of 30°. The flight tracks are about 12 km and 4 km long, respectively. Note that the frame 3 is very short and covers an area where, for calibration purposes, we have deployed 9 CRs and carried out DGPS measurements of their positions.

To process the data we have applied a standard SAR focusing [1] including the efficient two-step MOCO approach [6,7]. In particular, the MOCO corrections have been calculated by exploiting the SRTM external DEM. More specifically, to limit the effects induced by the beam-center

approximation [8] we have applied a 600 m × 400 m smoothing window to the SRTM data before calculating the MOCO corrections.

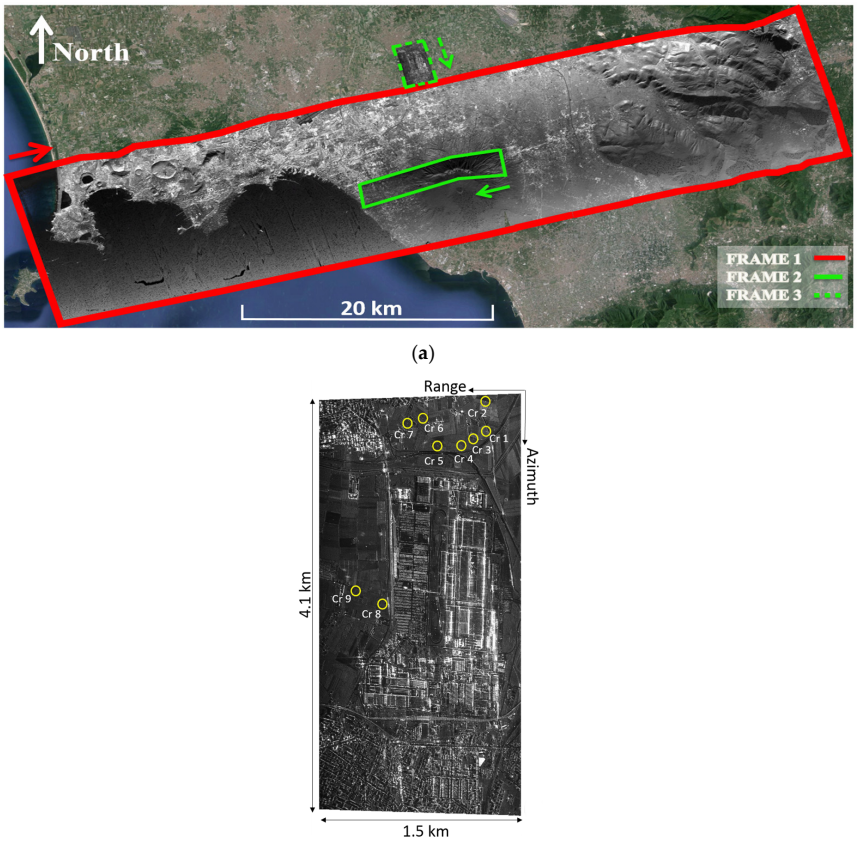

Figure 3. (**a**) Multi-look amplitude SAR images relevant to the acquired data. The frame n.1 (red) is relevant to the 50 MHz mode; the frame n.2 (continuous green) and the frame n.3 (dashed green) are relevant to the 400 MHz mode. The images are geocoded on a 5 × 5 m (50 MHz mode) and 1 × 1 m (400 MHz mode) geographic grid, and superimposed on a Google Earth image. The green and red arrows indicate the flight directions; (**b**) Amplitude SAR image (in the SAR coordinates grid) relevant to the frame n.3. A 4 range × 16 azimuth pixel averaging window has been applied, obtaining a 1.5 m × 1.85 m pixel spacing. The CRs deployed over the area are highlighted with yellow circles.

Table 5. SAR acquisitions.

	Frame 1	**Frame 2**	**Frame 3**
Bandwidth	50 MHz	400 MHz	400 MHz
Chirp pulses	1	4	4
Pulse duration	16.2 µs	2.6 µs	2.6 µs
Azimuth pixel spacing *	0.08 m	0.09 m	0.11 m
Azimuth resolution †	0.12 m	0.12 m	0.12 m
Range pixel spacing *	2.99 m	0.37 m	0.37 m
Range resolution †	3.84 m	0.48 m	0.48 m
Range lines	4096	4096	4096
Flight altitude	5001 m	3962 m	3962 m
Mean platform velocity	139 m/s	103 m/s	126 m/s
Look angle	30°–74°	30°–50°	30°–50°

* Raw data; † Theoretical.

In the 50 MHz case, we have also applied a 2 azimuth pixel presumming on the raw data [25]. Finally, we have applied a standard InSAR processing chain. In particular, to coregister the images we have applied a geometric approach [26] by exploiting again the SRTM external DEM.

In Figure 3a, the multi-look amplitude SAR images relevant to the three considered acquisitions have been geocoded [1] and superimposed to a Google Earth image. Note in particular that the 50 MHz and 400 MHz images have been reported on a 5 × 5 m and 1 × 1 m geographic grid, respectively. Figure 3a clearly shows the different peculiarities of the 400 MHz and the 50 MHz modes. The price paid to achieve the highest resolution is the reduction of the recorded range swath. With particular reference to the high resolution mode, Figure 3b reports also the SAR image (in the SAR coordinates grid) relevant to the frame 3, with the positions of the CRs highlighted. Note that the CRs are located at different range coordinates, covering the whole illuminated swath.

Turning to the InSAR products, Figure 4 shows, in the SAR coordinates grid, the interferogram and the coherence map relevant to the frame 1. In particular, a simple 24 azimuth pixel averaging has been applied to the interferogram just for visualization purposes (we have indeed obtained an almost square pixel of dimensions equal to 3 m × 4.18 m), without further application of phase noise filters, such as that in [27].

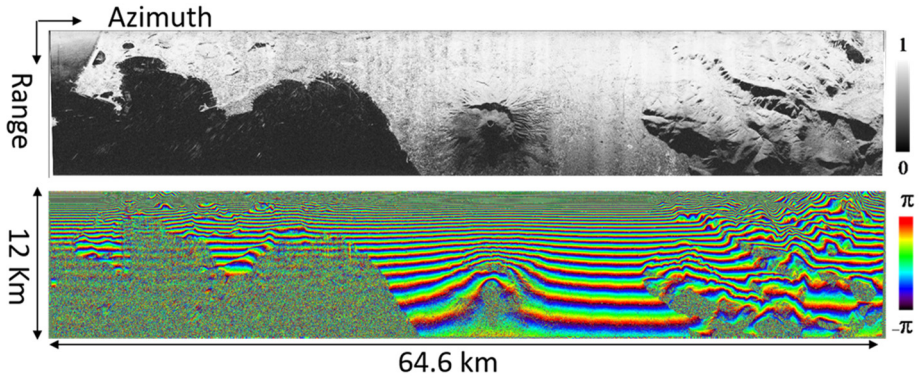

Figure 4. Coherence map and interferogram relevant to the frame 1 of Figure 3a (50 MHz mode, single-baseline configuration). The applied pixel averaging is described in the body of the paper.

From the top panel of Figure 4 it can be seen a coherence degradation in far range. In particular, we have measured a fast impairment of the mean coherence for incidence angles greater than approximately 60°. This is in agreement with the NESZ curves of Figure 1 and confirms that, as expected, only a part (corresponding approximately to the angular sector 30°–60°) of the recorded swath can be effectively exploited with the 50 MHz mode.

As for the full resolution mode, Figure 5 shows, in the SAR coordinates grid, two coherence maps and two interferograms relevant to the frame 2. In particular, we have considered the two data pairs with the largest (left panels) and the smallest (right panels) XT baselines. Again, we have just applied a simple pixel averaging window (2 range × 12 azimuth), in order to obtain an almost square pixel (0.75 m × 1.15 m). As expected from the NESZ curves of Figure 1, in this case both the single-pass interferograms are very coherent over the whole illuminated (range) swath.

For the 400 MHz mode we have performed a quantitative assessment of the obtained SAR products. To this aim, first of all we have exploited the in-field DGPS measurements on the nine CRs properly deployed within the frame 3. More specifically, we have carried out three kinds of measurements.

First, in the Single Look Complex (SLC) image we have measured the geometric resolution in correspondence of the nine CRs. The achieved results are listed in Table 6, whereas the expected values are 0.12 m in azimuth (we have processed a Doppler bandwidth equal to 920 Hz, which is about 20% wider than the half power one, see Section 2) and 0.48 m in range (by accounting for the

amplitude tapering of the transmitted chirp spectrum). In particular, we have measured a mean azimuth resolution of 0.14 m with a standard deviation of 0.02 m, and a mean range resolution of 0.49 m with a standard deviation of 0.01 m. It is remarked that to achieve the best spatial resolution, we have not applied any filtering (such as the Hamming one [1]) aimed at reducing the side lobe level of the point spread function because such filters also lead to a degradation of the resolution values. It is also noted that the measured resolutions are very close to the theoretical ones, but for the second CR, where we have a 75% degradation of the azimuth resolution.

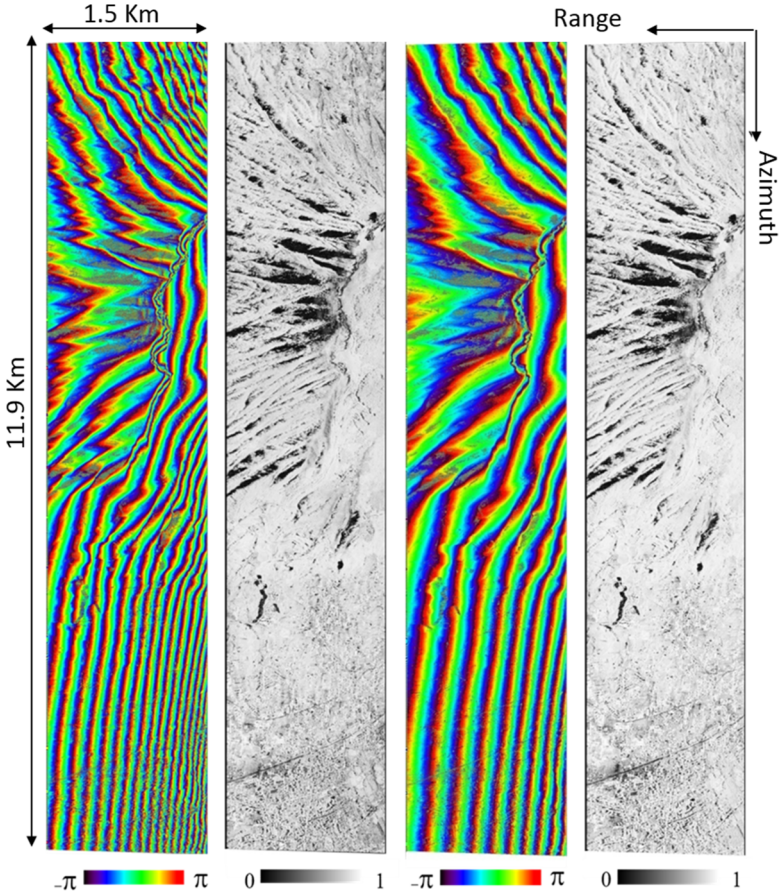

Figure 5. Two interferograms and the corresponding coherence maps relevant to the frame 2 of Figure 3a (400 MHz mode, multi-baseline configuration). Left panels refer to the data pair acquired with the largest XT baseline (height of ambiguity ranging from 44 m to 124 m). Right panels refer to the data pair acquired with the smallest XT baseline (height of ambiguity ranging from 87 m to 196 m). The applied pixel averaging is described in the body of the paper.

As the second experiment, we have applied the backward geocoding procedure [1] to the DGPS positions of the CRs, thus calculating their expected azimuth and range coordinates in the corresponding SAR coordinates grid. Then, we have compared such coordinates with those of the CRs imaged in the SLC image. The measured range and azimuth misalignments are listed in Table 6. In particular, we have measured a mean azimuth misalignment of 0.08 m with a standard deviation of 0.07 m, and a mean range misalignment of 0.04 m with a standard deviation of 0.08 m. The measured values are thus smaller than the corresponding geometric resolutions.

As the third experiment, we have evaluated the vertical accuracy of the obtained InSAR DEM. To this aim, we have considered only the largest baseline interferogram (joint exploitation of both the available interferograms, although possible [4], is beyond the aim of this work). We have then computed the unknown Phase Offset present in the unwrapped phase by applying the PBE

procedure [28] via the exploitation of the DGPS measurements on the CRs. Finally, we have carried out the phase-to-height conversion [1] and, in correspondence of the CR positions, we have compared the achieved heights with the DGPS ones. Results are again collected in Table 6; in particular, we have measured a mean vertical error of −0.08 m with a standard deviation of 0.51 m. It is noted that the height error collected in Table 6 seems to be affected by a linear trend along range. Typically, this may be an indication of a small baseline tilt error, which might come from a roll angle offset or limited accuracy in the estimation of the antenna phase centers. In our case, considering the high precision of the method exploited to calculate the antenna phase centers (see Section 2.1), it is likely that this baseline tilt error has been induced by a roll bias affecting the measurement of the IMU axes orientation. More specifically, such measurement has been carried out before the airborne missions (along with that of the antenna lever arms) with a Total Station Theodolite (TST). To this regard, it is noted that it has been quite difficult to reach the IMU box inside the airplane with the laser ray of the Electronic Distance Meter (EDM) integrated within the TST (which was instead located outside the airplane). This could have introduced inaccuracies in the IMU axes orientation measurement. However, since the whole radar has been dismounted just after the campaign, a deeper investigation of this issue requires the execution of other flight missions.

Table 6. Measurements on corner reflectors.

	Azimuth Resolution [m]	Range Resolution [m]	Azimuth Misalignment [m]	Range Misalignment [m]	Height Error [m]
CR 1	0.14	0.49	0.09	0.17	0.51
CR 2	0.21	0.50	0.02	0.16	0.47
CR 3	0.13	0.50	0.12	0.01	0.38
CR 4	0.13	0.50	0.08	0.09	0.28
CR 5	0.13	0.49	0.03	0.05	−0.20
CR 6	0.15	0.49	0.15	−0.03	−0.13
CR 7	0.14	0.52	0.13	0.01	−0.72
CR 8	0.12	0.48	0.14	−0.03	−0.78
CR 9	0.12	0.48	−0.07	−0.07	−0.53
μ	0.14	0.49	0.08	0.04	−0.08
σ	0.02	0.01	0.07	0.08	0.51

μ and σ indicate the mean and the standard deviation, respectively, of the achieved results.

To further assess the vertical accuracy of the InSAeS4 system, we have also performed an extended scene analysis. To this aim, we have exploited a laser scanner DEM relevant to the 3 km long area covered by the 1944 lava flow on the Somma Vesuvio volcanic complex [29]. In particular, such a DEM has been provided by the Osservatorio Vesuviano (OV) of the Istituto Nazionale di Geofisica e Vulcanologia (INGV). The test site is placed within the frames 1 and 2; however, for the 50 MHz acquisition (frame 1), it falls within a shadowing area. Accordingly, only comparison with the 400 MHz data (frame 2) has been possible: a zoom of the corresponding (geocoded) SLC is reported in Figure 6a with highlighted the test site (yellow). Again, we have exploited only the interferogram with the largest baseline. By comparing our InSAeS4 DEM and the available laser scanner one we have obtained the histogram reported in Figure 6b. In particular, we have measured a mean vertical error of 0.07 m with a standard deviation of 1.57 m. The latter result is thus worse than that obtained through the analysis carried out above by exploiting the CRs. To this regard, we note that the height of ambiguity relevant to the used baseline and the considered test area ranges from 75 m to 90 m. Accordingly, the standard deviation of the vertical error measured in the test area (1.57 m) turns out to be related to an interferometric phase error with standard deviation ranging approximately from 6° to 7°. Although this preliminary result is certainly fine, we are quite confident that it can be further improved, especially if we consider the vertical accuracy obtained in correspondence of the CRs. Indeed, the possible presence of the baseline tilt bias mentioned above, coupled with

the azimuth-variant attitude instabilities of the airplane during the acquisition, could have been responsible for the presence of residual phase errors in the corresponding single-pass interferogram. These in turn may have affected the final interferometric DEM along both the azimuth and the range directions. Further investigation of these issues will be addressed in the future by planning new InSAeS4 flight missions aimed at providing comparisons with available reference laser scanner DEMs wider than that exploited in this work and possibly relevant to different test sites characterized by different topographic features.

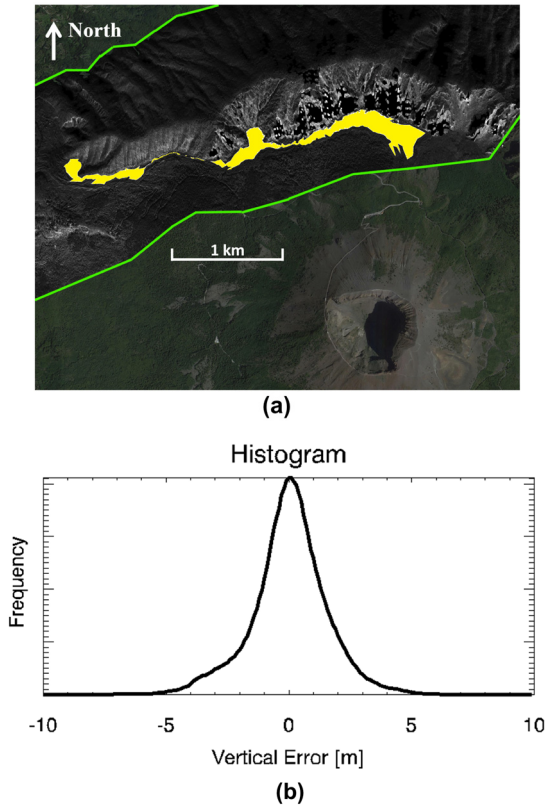

Figure 6. (**a**) Zoom of the frame 2 of Figure 3a. The lava flow erupted from the Somma Vesuvio volcanic complex in 1944 covered by the laser scanner DEM is highlighted in yellow; (**b**) Histogram of the vertical difference between the InSAeS4 DEM and the laser scanner DEM in the yellow area of Figure 6a.

4. Conclusions

The InSAeS4 is a new Italian airborne X-Band interferometric SAR, which upgrades the AeS4 sensor originally equipped with a single antenna. The system consists of three interferometric channels that allow carrying out both XT and AT interferometry; moreover, different operational modes characterized by different bandwidths and across-track swaths can be set.

In this work, we have provided a first assessment of the imaging and topographic mapping capabilities of the system, thus providing reference values for future research activities involving the exploitation of the data acquired by the sensor. In particular, measurements in correspondence of the CRs properly deployed in one illuminated area have shown that, in the 400 MHz case, we achieve mean geometric resolutions for the SLC images of 0.14 m (azimuth) $\times$ 0.49 m (range) with standard deviation of 0.02 m (azimuth) and 0.01 m (range). To assess the vertical accuracy of the single-pass InSAR DEM we have performed comparisons with the DGPS measurements on the CRs and with a laser scanner DEM, obtaining in the former case a mean vertical error of -0.08 m with a standard

deviation of 0.51 m, and in the latter one a mean vertical error of 0.07 m with a standard deviation of 1.57 m.

The exploitation of the AT interferometric configuration is a matter of current investigation and future work. Anyway, the presented results already show that the InSAeS4 may represent a key instrument for monitoring and surveillance of the Italian territory (although the system can be also operated abroad), especially in natural disaster scenarios, where the flexibility guaranteed by airborne radar acquisitions can profitably integrate satellite remote sensing data.

Acknowledgments: The authors thank AGEA, which has supported with IREA-CNR the InSAeS4 acquisition campaign; S. Guarino, F. Parisi and M. C. Rasulo of IREA-CNR, for their support; A. Gifuni of Università degli Studi di Napoli "Parthenope", for his contribution to the antennas measurements; G. De Angelis of e-GEOS, for the post-flight processing of the IMU data; G. Vilardo of OV-INGV for providing the laser scanner data; S. Trinca of Aeromanagement Europe, for his support during the flights; Prof. V. Cuomo for his efforts in the implementation of the cooperation between CNR and AGEA.

Author Contributions: The preparation of the work has been possible due to the cooperation between a public research Institute (CNR-IREA), public Universities (Parthenope-DI and Sannio-DING) and a private company (Bradar Indústria S/A). In particular, C.W. of Bradar and the researchers of CNR-IREA, Parthenope-DI and Sannio-DING (S.P., C.E., P.B., G.J., A.P. and R.L.) have mainly worked on the data processing and analysis; the other components of the Bradar team (T.A., J.M. and E.V.J.) have mainly worked on the realization of the system upgrade. The campaign has been prepared with the contribution of all the authors. In addition, S.P. and R.L. have supervised the entire work.

Conflicts of Interest: The authors declare no conflict of interest.

References

1. Franceschetti, G.; Lanari, R. *Synthetic Aperture Radar Processing*, 1st ed.; CRC Press: Boca Raton, FL, USA, 1999.
2. Bamler, R.; Hartl, P. Synthetic aperture radar interferometry. In *Inverse Problems*; IOP Publishing: Bristowl, UK, 1998; pp. R1–R54.
3. Rabus, B.; Eineder, M.; Roth, A.; Bamler, R. The shuttle radar topography mission—A new class of digital elevation models acquired by spaceborne radar. *ISPRS J. Photogramm. Remote Sens.* **2003**, *57*, 241–262. [CrossRef]
4. Krieger, G.; Moreira, A.; Fiedler, H.; Hajnsek, I.; Werner, M.; Younis, M.; Zink, M. TanDEM-X: A Satellite Formation for High-Resolution SAR Interferometry. *IEEE Trans. Geosci. Remote Sens.* **2007**, *45*, 3317–3341. [CrossRef]
5. Fornaro, G.; Franceschetti, G.; Perna, S. Motion Compensation errors: Effects on the accuracy of airborne SAR images. *IEEE Trans. Aerosp. Electron. Syst.* **2005**, *41*, 1338–1352. [CrossRef]
6. Fornaro, G. Trajectory Deviations in Airborne SAR: Analysis and Compensation. *IEEE Trans. Aerosp. Electron. Syst.* **1999**, *35*, 997–1009. [CrossRef]
7. Moreira, A.; Huang, Y. Airborne SAR Processing of highly squinted data using a chirp scaling approach with integrated motion compensation. *IEEE Trans. Geosci. Remote Sens.* **1994**, *32*, 1029–1040. [CrossRef]
8. Fornaro, G.; Franceschetti, G.; Perna, S. On Center Beam Approximation in SAR Motion Compensation. *IEEE Geosci. Remote Sens. Lett.* **2006**, *3*, 276–280. [CrossRef]
9. Perna, S.; Wimmer, C.; Moreira, J.; Fornaro, G. X-Band Airborne Differential Interferometry: Results of the OrbiSAR Campaign over the Perugia Area. *IEEE Trans. Geosci. Remote Sens.* **2008**, *46*, 489–503. [CrossRef]
10. Shiroma, G.H.X.; de Macedo, K.A.C.; Wimmer, C.; Fernandes, D.; Barreto, T.L.M. Combining dual-band capability and polinsar technique for forest ground and canopy estimation. In Proceedings of the International Geoscience and Remote Sensing Symposium, Quebec City, QC, Canada, 13–18 July 2014.
11. Hensley, S.; Chapin, E.; Freedman, A.; Le, C.; Madsen, S.; Michel, T.; Rodriguez, E.; Siqueira, P.; Wheeler, K. First P-band results using the Geosar mapping system. In Proceedings of the International Geoscience and Remote Sensing Symposium, Sydney, Australia, 9–13 July 2001.
12. Horn, R.; Nottensteiner, A.; Reigber, A.; Fischer, J.; Scheiber, R. F-SAR—DLR's new multifrequency polarimetric airborne SAR. In Proceedings of the International Geoscience and Remote Sensing Symposium, Cape Town, South Africa, 12–17 July 2009.

13. Brenner, A.R.; Roessing, L. Radar Imaging of Urban Areas by Means of Very High-Resolution SAR and Interferometric SAR. *IEEE Trans. Geosci. Remote Sens.* **2008**, *46*, 2971–2982. [CrossRef]
14. Dubois-Fernandez, P.; du Plessis, O.R.; le Coz, D.; Dupas, J.; Vaizan, B.; Dupuis, X.; Cantalloube, H.; Coloumbeix, C.; Titin-Schnaider, C.; Dreuillet, P.; *et al.* The ONERA RAMSES SAR System. In Proceedings of the International Geoscience and Remote Sensing Symposium, Toronto, ON, Canada, 24–28 June 2002.
15. Ruault du Plessis, O.; Nouvel, J.; Baque, R.; Bonin, G.; Dreuillet, P.; Coulombaix, C.; Oriot, H. ONERA SAR facilities. *IEEE Aerosp. Electron. Syst. Mag.* **2011**, *26*, 24–30. [CrossRef]
16. Magnard, C.; Frioud, M.; Small, D.; Brehm, T.; Essen, H.; Meier, E. Processing of MEMPHIS Ka-Band Multibaseline Interferometric SAR Data: From Raw Data to Digital Surface Models. *IEEE J. Sel. Top. Appl. Earth Observ. Remote Sens.* **2014**, *7*, 2927–2941. [CrossRef]
17. Schmitt, M.; Magnard, C.; Stanko, S.; Ackermann, C.; Stilla, U. Advanced high resolution SAR interferometry of urban areas with airborne millimetrewave radar. *Photogramm. Fernerkund. Geoinform.* **2013**, *6*, 603–617. [CrossRef]
18. Schmitt, M.; Magnard, C.; Brehm, T.; Stilla, U. Towards airborne single pass decimeter resolution SAR interferometry over urban areas. In *Photogrammetric Image Analysis*; Springer-Verlag Berlin: Heidelberg, Germany, 2011; pp. 197–208.
19. Magnard, C.; Frioud, M.; Small, D.; Brehm, T.; Meier, E. Analysis of a Maximum Likelihood Phase Estimation Method for Airborne Multibaseline SAR Interferometry. *IEEE J. Sel. Top. Appl. Earth Observ. Remote Sens.* **2015**. in press. [CrossRef]
20. Schmitt, M.; Stilla, U. Maximum-likelihood based approach for single-pass synthetic aperture radar tomography over urban areas. *IET Radar Sonar Navig.* **2014**, *8*, 1145–1153. [CrossRef]
21. Perna, S.; Berardino, P.; Britti, F.; Cirillo, C.; Esposito, C.; Fornaro, G.; Lubeck, D.; Monaldi, G.; Moreira, J.; Pauciullo, A.; *et al.* Capabilities of the TELAER Airborne SAR System Upgraded to the Multi-Antenna Mode. In Proceedings of the International Geoscience and Remote Sensing Symposium, Munich, Germany, 22–27 July 2012.
22. Balanis, C.A. *Antenna Theory: Analysis and Design*, 3rd ed.; Wiley-Interscience: New York, NY, USA, 2005.
23. Perna, S.; Esposito, C.; Pauciullo, A.; Romano, P.; Gifuni, A. A fast approach for antenna phase center evaluation. In Proceedings of the International Geoscience and Remote Sensing Symposium, Quebec City, QC, Canada, 13–18 July 2014.
24. Richards, M.A.; Scheer, J.A.; Holm, W.A. *Principles of Modern Radar: Basic Principles*; SciTech Publishing: Raleigh, NC, USA, 2010.
25. Massonnet, D.; Adragna, F.; Rossi, M. CNES General-Purpose SAR Correlator. *IEEE Trans. Geosci. Remote Sens.* **1994**, *32*, 636–643. [CrossRef]
26. Sansosti, E.; Berardino, P.; Manunta, M.; Serafino, F.; Fornaro, G. Geometrical SAR image registration. *IEEE Trans. Geosci. Remote Sens.* **2006**, *44*, 2861–2870. [CrossRef]
27. Goldstein, R.M.; Werner, C.L. Radar interferogram filtering for geophysical applications. *Geophys. Res. Lett.* **1998**, *25*, 4035–4038. [CrossRef]
28. Perna, S.; Esposito, C.; Berardino, P.; Pauciullo, A.; Wimmer, C.; Lanari, R. Phase Offset Calculation for Airborne InSAR DEM Generation Without Corner Reflectors. *IEEE Trans. Geosci. Remote Sens.* **2014**, *53*, 2713–2726. [CrossRef]
29. Vilardo, G.; Ventura, G. Geomorphological map of the 1944 Vesuvius lava flow (Italy). *J. Maps* **2008**, *4*, 225–234. [CrossRef]